

Article

Development of a Novel Microgap Reactor System for the Photocatalytic Degradation of Micropollutants from Aqueous Solutions with TiO₂-Based Photocatalysts Immobilized by Spray Coating

Tony B. Engelhardt, Minrui Zhu, Claudia Heilmann, Sabine Schmitz-Stöwe, Thomas Schwarz and Klaus Stöwe *

Institut für Chemie, Fakultät für Naturwissenschaften, Technische Universität Chemnitz, 09111 Chemnitz, Germany; tony-benjamin.engelhardt@s2012.tu-chemnitz.de (T.B.E.); minrui.zhu@s2017.tu-chemnitz.de (M.Z.); claudia.heilmann@mvtat.tu-freiberg.de (C.H.); sabine.schmitz-stoewe@chemie.tu-chemnitz.de (S.S.-S.); thomas.schwarz@chemie.tu-chemnitz.de (T.S.)
* Correspondence: klaus.stoewe@chemie.tu-chemnitz.de; Tel.: +49-371-531-21270



Citation: Engelhardt, T.B.; Zhu, M.; Heilmann, C.; Schmitz-Stöwe, S.; Schwarz, T.; Stöwe, K. Development of a Novel Microgap Reactor System for the Photocatalytic Degradation of Micropollutants from Aqueous Solutions with TiO₂-Based Photocatalysts Immobilized by Spray Coating. *Catalysts* **2021**, *11*, 1351.
<https://doi.org/10.3390/catal11111351>

Academic Editor: Detlef W. Bahnemann

Received: 26 October 2021

Accepted: 8 November 2021

Published: 11 November 2021

Publisher's Note: MDPI stays neutral with regard to jurisdictional claims in published maps and institutional affiliations.



Copyright: © 2021 by the authors. Licensee MDPI, Basel, Switzerland. This article is an open access article distributed under the terms and conditions of the Creative Commons Attribution (CC BY) license (<https://creativecommons.org/licenses/by/4.0/>).

Abstract: The presented investigation focuses on the development of a novel microgap reactor concept for the photocatalytic degradation of micropollutants from aqueous solutions with titanium dioxide-based catalysts immobilized by spray coating. Combinatorial experiment designs were utilized in order to study the influence of the microgap width, irradiance and catalyst layer thickness on the conversion of 17 α-ethinyl estradiol. The impact of catalyst-doping is discussed as well. Regarding conversion analyses, LC-MS/MS and GC-MS techniques were deployed, while XRD, ESEM and BET were utilized for catalyst characterization. The results show that the built-up microgap reactor system enables a conversion of 65% within a residence time of 2.7 min with UV-A irradiation and under steady flow conditions. Thus, the presented bench scale photocatalysis reactor provides promising fundamental findings for the future development of pilot scale approaches. With the deployment of industrial catalysts and base materials, microgap reactor photocatalytic degradation represents an attractive technology for large-scale application.

Keywords: microgap reactor; photocatalysis; TiO₂; P25; endocrine disruptors; UHPLC-MS/MS

1. Introduction

In addressing one of the biggest global challenges, i.e., climate change, humankind must seek to minimize numerous activities which have a negative impact on the environment [1–5]. Demand for already scarce freshwater reserves will increase further, as extreme weather events, which are becoming more and more common, have the potential to contaminate freshwater reservoirs or cause essential rain precipitation to fall out. The increasing carbon dioxide content in the atmosphere [6] enables plants to grow larger and increases their lifespan, leading them to consume and hold greater amounts of fresh water, thereby worsening the disparity between fresh water consumption and recovery. Fresh water as a commodity will increase in value in the future, and will be more fought over than it is nowadays [7]. Thus, wastewater treatment will play an important role worldwide, as is already the case in the West. With the objectives of providing the population with water which is as containment free as possible and purifying domestic water for discharge into the natural environment, additions to existing and widely deployed activated sludge wastewater treatment techniques, for example advanced oxidation processes (AOPs), have been extensively discussed [8–11]. One category of AOP makes use of photocatalysis [12], whereby a semiconducting material such as titanium dioxide is irradiated with light of a particular wavelength ($\lambda < 390$ nm for TiO₂), for example UV-A irradiation. Highly energetic irradiation enables the electrons of the photocatalyst valence band to pass the material band gap (E_g , anatase = 3.2 eV [13]) and reach an excited state in the conduction

band, leaving a positively charged hole in the valence band. In this way, the newly-formed electron-hole pairs act as excitons and facilitate redox reactions on the catalyst surface. The unresponsive recombination of electron-hole pairs represents a challenge with regard to this cohesion, as it prohibits photocatalytic activity. Therefore, efforts have been made in catalyst research to inhibit recombination and keep the material in an active state as much as possible. This may be achieved, for example, by transition metal doping for the build-up of surface defects formed by oxygen vacancies, leading to enhanced charge separation and increased exciton stability [14–18]. While research on photocatalytic materials has advanced significantly in recent decades, technologies allowing the application of photocatalysis to wastewater treatment processes are largely lacking [19,20]. Therefore, this publication investigates of a novel microgap reactor concept, deploying titanium dioxide-based catalysts immobilized by spray coating and UV-A irradiation for the photocatalytic degradation of micropollutants from aqueous solutions. For this study, hormonal contraceptive 17 α -ethynodiol (EE2) was chosen as target molecule, as it is a persistent contaminant of surface water which negatively affects wildlife, i.e., it functions as endocrine disruptor, at below ppb concentrations [21–24]. The influence of various reactor parameters, such as the microgap width, irradiance, catalyst layer thickness and catalyst-doping, are investigated and discussed in this paper.

2. Results

2.1. Calibration

Information regarding the calibration of the system is presented in Figures 1 and 2 and Table 1. These data reveal satisfactory linearity across the concentration range of interest, as well as a low process standard deviation (PSD) and limit of quantification (LOQ). The utilization of gas chromatography with mass spectrometry coupling (GC-MS) and ultrahigh performance liquid chromatography with tandem mass spectrometry coupling (UHPLC-MS/MS) was necessary in order to capture a wide range of analyte concentrations. The GC-MS was deployed with highly concentrated samples in order to determine the optimal experimentation parameters for the microgap reactor. The limit of this procedure was determined by the obligatory trimethylsilyl-derivatization, which failed to quantitatively convert EE2 into its derivative at low concentrations ($c < 1 \text{ mg L}^{-1}$). Concerning lower concentrations, a tandem mass spectrometer provided especially high signal-to-noise ratios in the MRM experiments. In addition, the utilization of a UHPLC as well as an electron spray ion source facilitated the application of native samples, i.e., aqueous estrogen solutions, without any derivatization. These observations led to the prioritization of UHPLC-MS/MS over GC-MS quantitation, especially for samples with a low concentration of aqueous estrogen.

2.2. Catalyst Characterization

In the powder x-ray diffraction (XRD) measurements, P25 showed a phase composition of $81.4 \pm 0.8\%$ anatase and $18.4 \pm 0.2\%$ rutile, which was not influenced by the chosen parameters during calcination. Since the temperature for the phase transition of anatase to rutile has been reported in the literature as $\vartheta_{\text{transition}} = 600 \text{ }^{\circ}\text{C}$ [25], and as it was our intention to preserve the amount of anatase present due to its higher photocatalytic activity compared to rutile [26], proper calcination conditions were applied. Following a second calcination of the already calcined P25 in the presence of binder and ethylene glycol, it was found that the phase composition did not change, just as is observed during copper-doping (see Figure 3, Table 2). While low amounts of copper-doping seemed not to influence the phase composition, coherence between the degree of copper doping and the lattice parameters was found for both polymorphs of titanium dioxide, anatase and rutile, but especially for the former, in which the presence of copper ions enlarged the lattice parameters (see Figure 4). This phenomenon could be explained by the fact that the substituting copper (II) ions are significantly larger than titanium (IV) ions [27], and to

preserve charge neutrality, additional Cu^{2+} ions have to be incorporated at interstitial sites in order to avoid the introduction of oxygen vacancies.

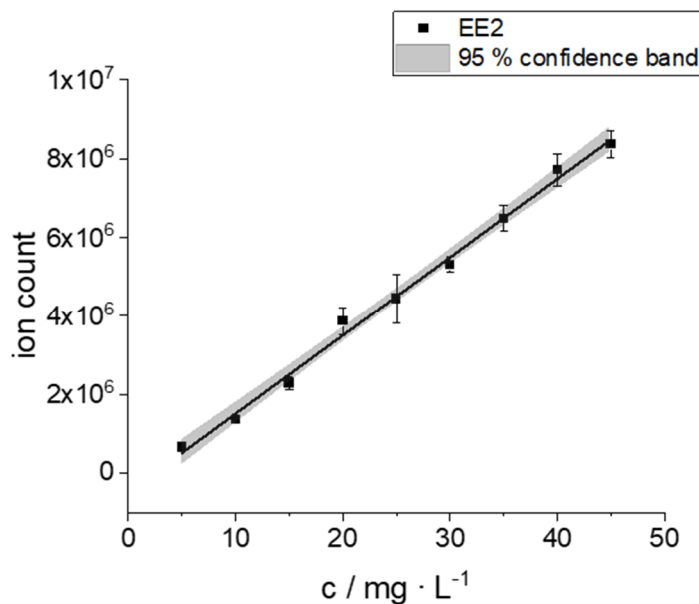


Figure 1. Calibration curve formed by GC-MS measurements of nine calibration standards ranging from $c = 5 \text{ mg L}^{-1}$ to $c = 45 \text{ mg L}^{-1}$ with an increment of $\Delta c = 5 \text{ mg L}^{-1}$; quintuple determination; linear regression, slope: $199,271.79 \text{ L mg}^{-1} \pm 5681.07 \text{ L mg}^{-1}$, point of intersection with the ordinate: $-481,783.45 \pm 159,845.77$, $R^2 = 0.997$; ion counts determined by the integration of the EE2 signal in the obtained EIC chromatograms (EIC = extracted-ion current; precursor ions: 440 m/z , 425 m/z); concentration values represent the EE2 concentration in aqueous solution during the catalytic experiments.

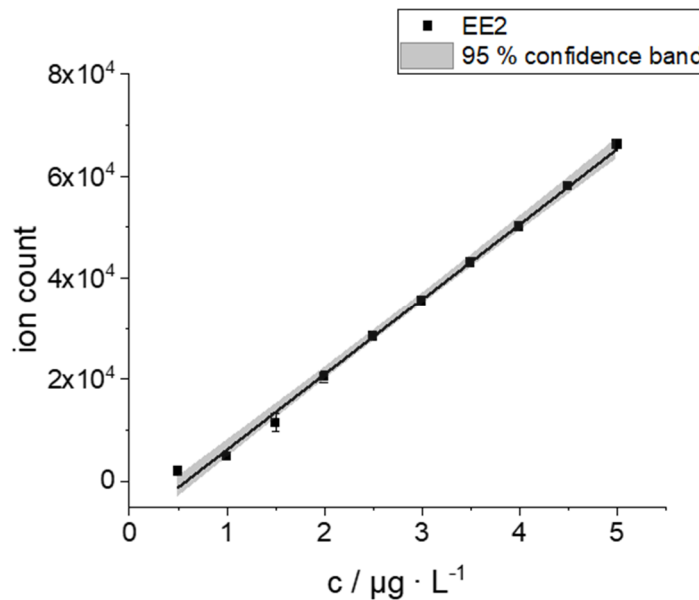


Figure 2. Calibration curve formed by UHPLC-MS/MS measurements of ten calibration standards ranging from $c = 0.5 \mu\text{g L}^{-1}$ to $c = 5 \mu\text{g L}^{-1}$ with an increment of $\Delta c = 0.5 \mu\text{g L}^{-1}$; quintuple determination; linear regression, slope: $14,771.11 \pm 325.04 \text{ L } \mu\text{g}^{-1}$, point of intersection with the ordinate: -8580.63 ± 1008.42 , $R^2 = 0.998$; ion counts determined by the integration of the respective EE2 signal in the obtained TIC chromatograms of MRM (TIC = total-ion current; see Table 3 for information on the precursor ion); the concentration values given represent the EE2 concentrations in aqueous solution during the catalytic experiments.

Table 1. Values for process standard deviation (PSD), limit of detection (LOD) and limit of quantitation (LOQ) in reference to Figures 1 and 2; according to DIN 32645.

System	PSD/ $\mu\text{g L}^{-1}$	LOD/ $\mu\text{g L}^{-1}$	LOQ/ $\mu\text{g L}^{-1}$
GC-MS	1.10×10^3	2.84×10^3	5.68×10^3
UHPLC-MS/MS	0.099	0.69	1.39

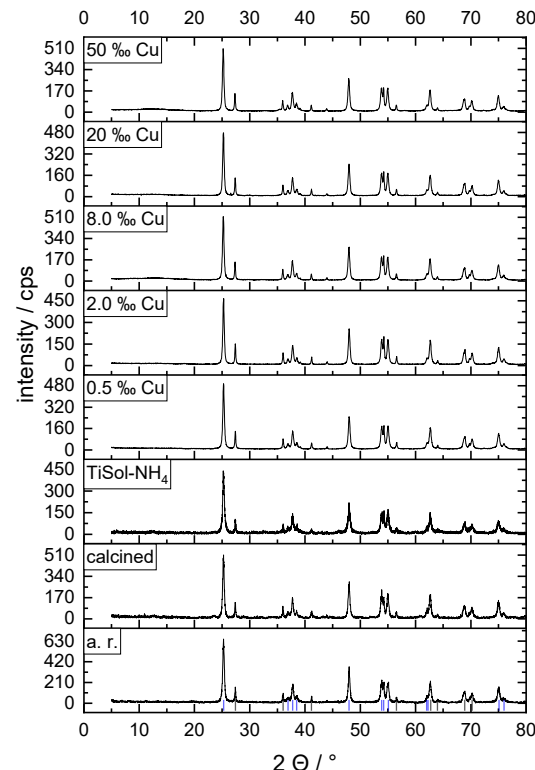


Figure 3. Powder X-Ray diffraction (XRD) pattern of different P25 samples; a. r.: P25 as received; calcined: $\vartheta = 500^\circ\text{C}$, $t = 2\text{ h}$; TiSol-NH₄: calcined P25 [$m = 150\text{ mg}$] combined with binder [$V = 1\text{ mL}$] and ethylene glycol [$V = 50\text{ }\mu\text{L}$] and calcined; 0.5% Cu—50% Cu: a. r. P25 impregnated with copper acetate solution [$x_{\text{Cu}} = 0.5, 2, 8, 20, 50\%$; $x = n_{\text{Cu}} n_{\text{Ti}}^{-1}$] and calcined; at the bottom, there is a reference diffraction pattern according to ICDD: anatase (ICDD 73-1764)—blue, rutile (ICDD 73-1765)—black.

Table 2. Lattice parameters and phase composition, based on the Rietveld method for the crystalline anatase-type and rutile-type phase of different P25 samples, according to the XRD measurements (Figure 3); a. r.—P25 as received; calcined ($\vartheta = 500^\circ\text{C}$, $t = 2\text{ h}$); TiSol-NH₄ (calcined P25 [$m = 150\text{ mg}$] combined with binder [$V = 1\text{ mL}$] and ethylene glycol [$V = 50\text{ }\mu\text{L}$] and calcined; 0.5% Cu—50% Cu (a. r. P25 impregnated with copper acetate solution [$x_{\text{Cu}} = 0.5, 2, 8, 20, 50\%$; $x = n_{\text{Cu}} n_{\text{Ti}}^{-1}$] and calcined).

Sample	Lattice Parameters/Å						
	Phase Composition/wt. %			Anatase		Rutile	
	Anatase	Rutile	a	c	a	c	
a. r.	84.54 ± 0.85	15.46 ± 0.15	3.7836(2)	9.5042(6)	4.5929(3)	2.9572(4)	
calcined	83.19 ± 0.83	16.81 ± 0.17	3.7841(3)	9.5057(7)	4.5927(4)	2.9587(4)	
TiSol-NH ₄	87.60 ± 0.88	12.40 ± 0.12	3.7851(7)	9.506(2)	4.5935(8)	2.9593(6)	
0.5% Cu	82.69 ± 0.83	17.31 ± 0.17	3.7841(1)	9.5046(1)	4.5929(1)	2.9579(1)	
2.0% Cu	80.46 ± 0.80	19.54 ± 0.20	3.7840(1)	9.5056(1)	4.5929(1)	2.9579(1)	
8.0% Cu	82.53 ± 0.83	17.47 ± 0.17	3.7839(1)	9.5047(1)	4.5925(1)	2.9578(1)	
20% Cu	80.86 ± 0.81	19.14 ± 0.19	3.7842(1)	9.5051(1)	4.5928(1)	2.9579(1)	
50% Cu	82.28 ± 0.82	17.72 ± 0.18	3.7843(1)	9.5039(1)	4.5929(1)	2.9579(1)	

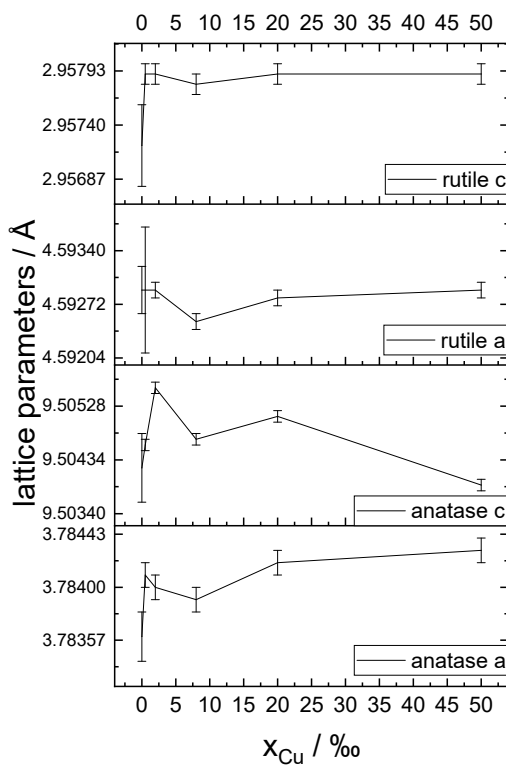
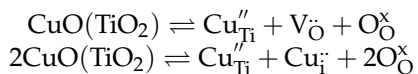


Figure 4. Lattice parameters of the crystalline anatase-type and rutile-type phase of different P25 samples doped with varying amounts of copper (P25 impregnated with copper acetate solution [$x_{\text{Cu}} = 0.5, 2, 8, 20, 50\%$; $x_{\text{Cu}} = n_{\text{Cu}} n_{\text{Ti}}^{-1}$] and calcined), according to the XRD measurements and Rietveld refinements of the diffraction data (see Figure 3, Table 2).



This finding strongly implies that the interdiffusion of copper ions has taken place into the crystal lattice of anatase, and probably also rutile. With the aim of investigating the influence of calcination temperature on the surface properties of P25, Brunauer-Emmett-Teller (BET) adsorption and desorption isotherms were determined, as shown in Figure 5. Concerning the specific surface area of P25 ($\text{SSA}_{\text{BET}, \text{P25}} = 33.83 \text{ m}^2 \text{ g}^{-1} \pm 0.33 \text{ m}^2 \text{ g}^{-1}$), an increase during calcination ($\text{SSA}_{\text{BET}, \text{P25, calc.}} = 50.18 \pm 0.50 \text{ m}^2 \text{ g}^{-1}$), and a further increase after second calcination in the presence of the binder and ethylene glycol ($\text{SSA}_{\text{BET}, \text{P25, calc.} + \text{TiSol-NH}_4} = 56.61 \pm 0.57 \text{ m}^2 \text{ g}^{-1}$), were determined. Comparing the shapes of the obtained BET adsorption and desorption isotherms with the IUPAC specifications [28], it was concluded that nonporous materials had been obtained (P25 is synthesized by flame spray pyrolysis), with the data indicating the formation of layer structures (Figure 5III). This was supported by environmental scanning electron microscopy (ESEM) images in combination with EDX scans, which clearly showed layer structures along the fractured surfaces of the mud crack structure (see Figure 6II). Doping with small amounts of copper did not influence the appearance of the obtained catalysts. Regarding the homogeneity of the applied copper, differences were discovered between the various layer preparation procedures (see Figure 7). With impregnation before spray coating, according to the EDX images, the copper ions stuck to the P25 during the shrink-triggered cracking of the surface, and therefore, did not appear within the gaps between the chunks (Figure 7Ib). If the substrate was impregnated after spray coating, immobilization copper appeared not only on the P25 surface, but also within the cracks of the mud crack structure, since it was sprayed on the already cracked surface, resulting in a more homogenous spread of copper (Figure 7IIb).

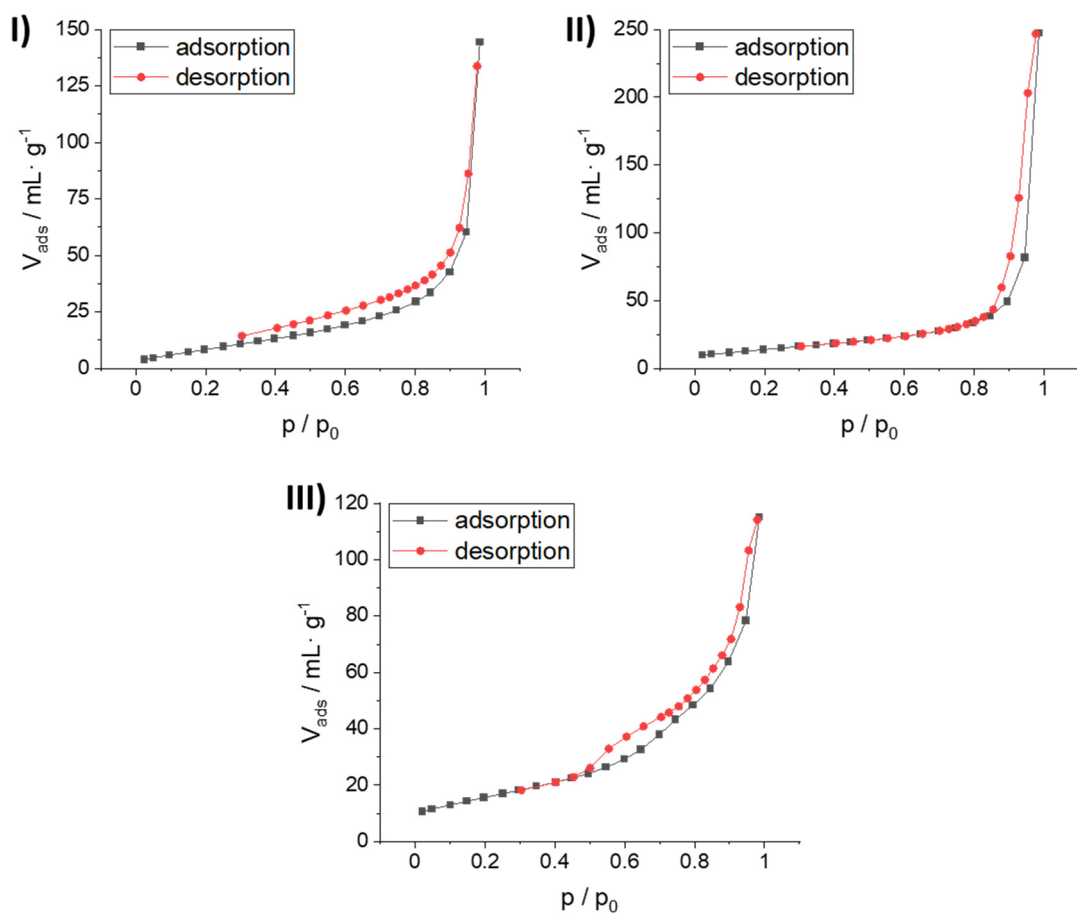


Figure 5. Adsorption (black) and desorption (red) isotherms based upon N₂ gas physisorption measurements according to BET; NOVAtouch 4LX, Quantachrome Instruments; (I) P25, as received, (II) P25 calcined, $\vartheta = 500$ °C, $t = 2$ h, pounded and sifted ($d < 100$ µm), (III) P25 (II), combined with Nyacol® TiSol-NH₄ binder and ethylene glycol, calcined again, $\vartheta = 500$ °C, $t = 2$ h, pounded and sifted ($d < 100$ µm). Isotherm shape indicates the presence of nonporous particle powders for (I) and (II), and shows signs of layer structures for (III), according to IUPAC [28].

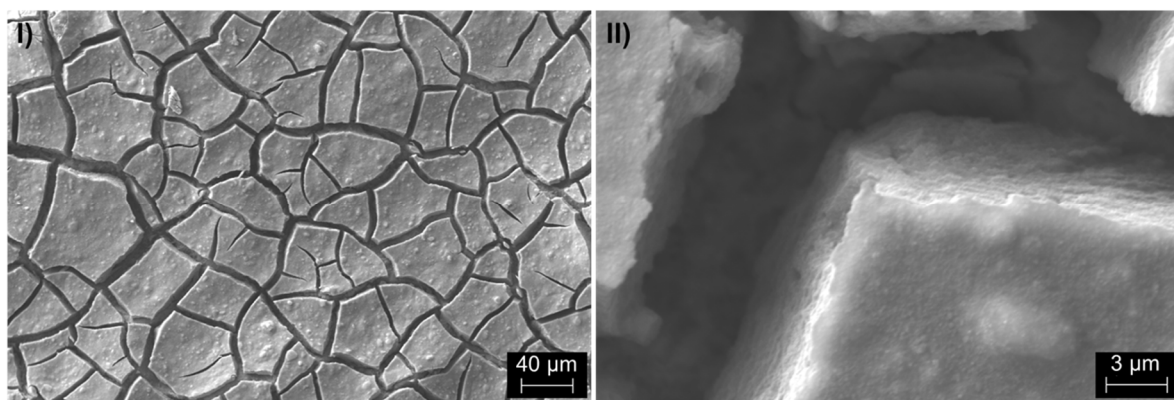


Figure 6. Environmental scanning electron microscopy images of P25 immobilized by spray coating on a rough steel substrate; U = 15 kV, I = 1.4 nA, high vacuum, 250-fold magnification (I) and 4 k-fold magnification (II).

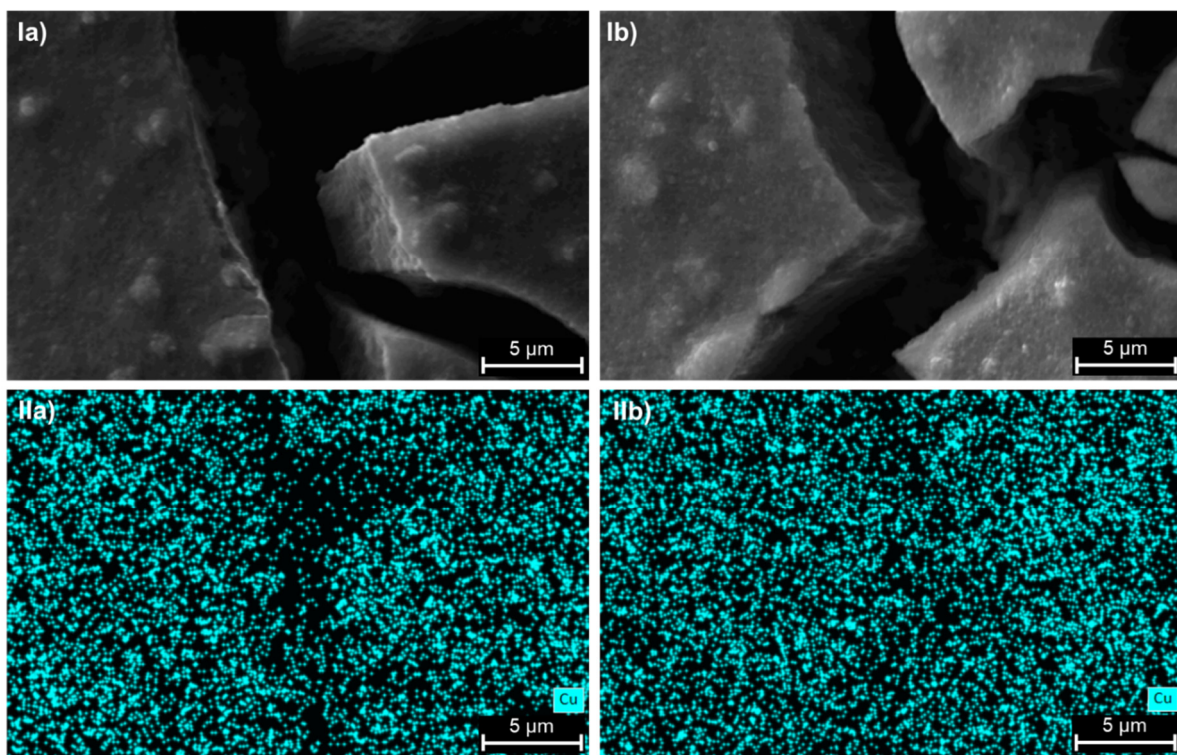


Figure 7. Environmental scanning electron microscopy images of copper-doped P25 immobilized by spray coating ($(x_{Cu} = n_{Cu} n_{Ti}^{-1} \approx 2\%)$) on a rough steel substrate (I), $U = 15$ kV, $I = 1.4$ nA, high vacuum, 4k-fold magnification; EDX element mapping of copper is given (II); comparison of two different preparation techniques: (a) impregnation before immobilization by spray coating; and (b) impregnation after immobilization by spray coating.

2.3. Optimization of Photocatalysis Parameters

Figure 8 presents the results of three combinatorial designs (I, II, III). The conversions of EE2 (X_{EE2}) determined according to Equation (1) (a), and the calculated effects of the chosen parameters (x_1, x_2, x_3), as well as their synergies and respective dyssynergies (interactions $x_1x_2, x_1x_3, x_2x_3, x_1x_2x_3$), are given (b). Positive effect values indicate an enhancement of the objective variable (X_{EE2}) regarding the considered parameter. The outcome of the first design (I) showed that besides the residence time (x_1), none of the other chosen parameters (x_2, x_3) yielded any significant effect, i.e., neither synergies nor dyssynergies. Regarding the conversion values, this coherence can also be seen in the significant effect of this parameter, despite the fact that the vastly differing amounts of catalyst in these experiments would be expected to give rise to varying conversions. An explanation for this occurrence could be that the system was in a state of mass transport limitation under the experimental conditions. Because of this coherence, the catalyst mass and the average catalyst layer thickness were drastically decreased in subsequent designs. The maximum residence time was also reduced ($\tau_+ = 2.0\text{--}1.0$ min) in order to diminish its effect and positively influence its ratio with the effects of the other parameters. The subsequent combinatorial design (II) showed satisfactory results concerning the effect ratios, since from the outcomes, the influence of each chosen parameter could now easily be quantified. Furthermore, the system seemed to be no longer in a mass transport limiting state with the chosen parameter values. In fact, varying catalyst masses appeared to alter the EE2 conversions. Most importantly, it is shown that thin catalyst layers ($d_{avg.} \approx 10$ μm) should be preferred over thicker ones. This cohesion aroused the suspicion that the reactor gap width and film thickness should be parameters under investigation; thus, these variables were assessed, along with the residence time, in the third design (III). This was because the study of the residence time provided rather obvious results. Regarding design III, during which the modified residence time (τ_{mod}), determined

according to Equation (2), remained constant, the film thickness indeed had an influence on the EE2 conversion; it was observed that thinner liquid films are superior to thicker ones. However, thinner films, such as the one tested ($d_{\text{film}} = 250 \mu\text{m}$), were not realizable due to leakage of the reactant solution. Again, the results showed that low amounts of catalyst should be favored; in contrast, the layers, which were too thin to be properly characterized by thickness measurements, were inadequate for testing. Thus, low catalyst masses ($m_{\text{P25}} \approx 100 \text{ mg}$) were chosen for future experiments. Irradiance with a thin catalyst layer and film had little to no impact on the objective variable within the tested range. Thus, for future experiments, the lowest value was chosen due to the higher overall electrical power consumption at higher irradiances.

$$X_{\text{EE2}} = 1 - \frac{n_{\text{EE2},t}}{n_{\text{EE2},0}} \quad (1)$$

$$\tau_{\text{mod}} = \frac{m_{\text{catalyst}}}{Q} \quad (2)$$

2.4. Start-Up Behavior

To determine the amount of pumped-through reactant solution required to reach an equilibrium state of conversion during photocatalysis, an experiment was performed in which solution samples pumped through the reactor were gathered from the start of the experimentation set. The results (shown in Figure 9) indicated that the chosen volume ($V_{\text{waste}} = 10 \text{ mL}$), obtained before collecting a sample, was adequate, as the pumped-through volume until equilibrium closely resembled the inherent dead volume of the reactor ($V_{\text{dead-volume}} \approx 4 \text{ mL}$).

2.5. Macro Kinetics of EE2 Degradation

To investigate the photocatalytic degradation mechanism of EE2 in the microgap reactor, an experiment in a 60-fold parallel stirring UV-A LED photoreactor system [29] in the presence of scavenger substances, i.e., potassium bromate, sodium iodide and tertiary butanol, was performed. The results of these investigations are presented in Figure 10. According to Abramović [30], these scavengers fulfill certain roles during the photocatalytic reaction. The iodide and bromate anions enrich themselves on the catalyst surface, while tertiary butyl alcohol is not as surface active, and therefore, is mainly located in the solution bulk. Regarding this coherence, the iodide ions react with excited electrons on the catalyst surface, while the bromate ions react with the electron holes formed during the photoexcitation of electrons in the semiconducting P25. Ultimately, tertiary butanol scavenges hydroxyl radicals formed by a photocatalytic reaction with water and oxygen, as further illustrated in Scheme 1. The degradation behavior of the EE2 in the presence of these agents in the reaction solution allowed us to draw conclusions about the location of its degradation reaction, i.e., either on the surface or in the solution bulk. As depicted in Figure 10, both sodium iodide and potassium bromate amplified the degradation rate, in comparison to the sample without additives. On the other hand, t-butanol inhibited the degradation to a point where it no longer followed a pseudo first order kinetic. It was concluded that the EE2 had been degraded by the reaction with hydroxyl radicals in the solution bulk. During the continuous irradiation of a steady estrogen solution flow through the reactor, a relatively large quantity ($V = 20 \text{ mL}$) of solution in an equilibrated state was gathered for dissolved oxygen determination. During this process, oxygen was consumed, as indicated in Figure 11.

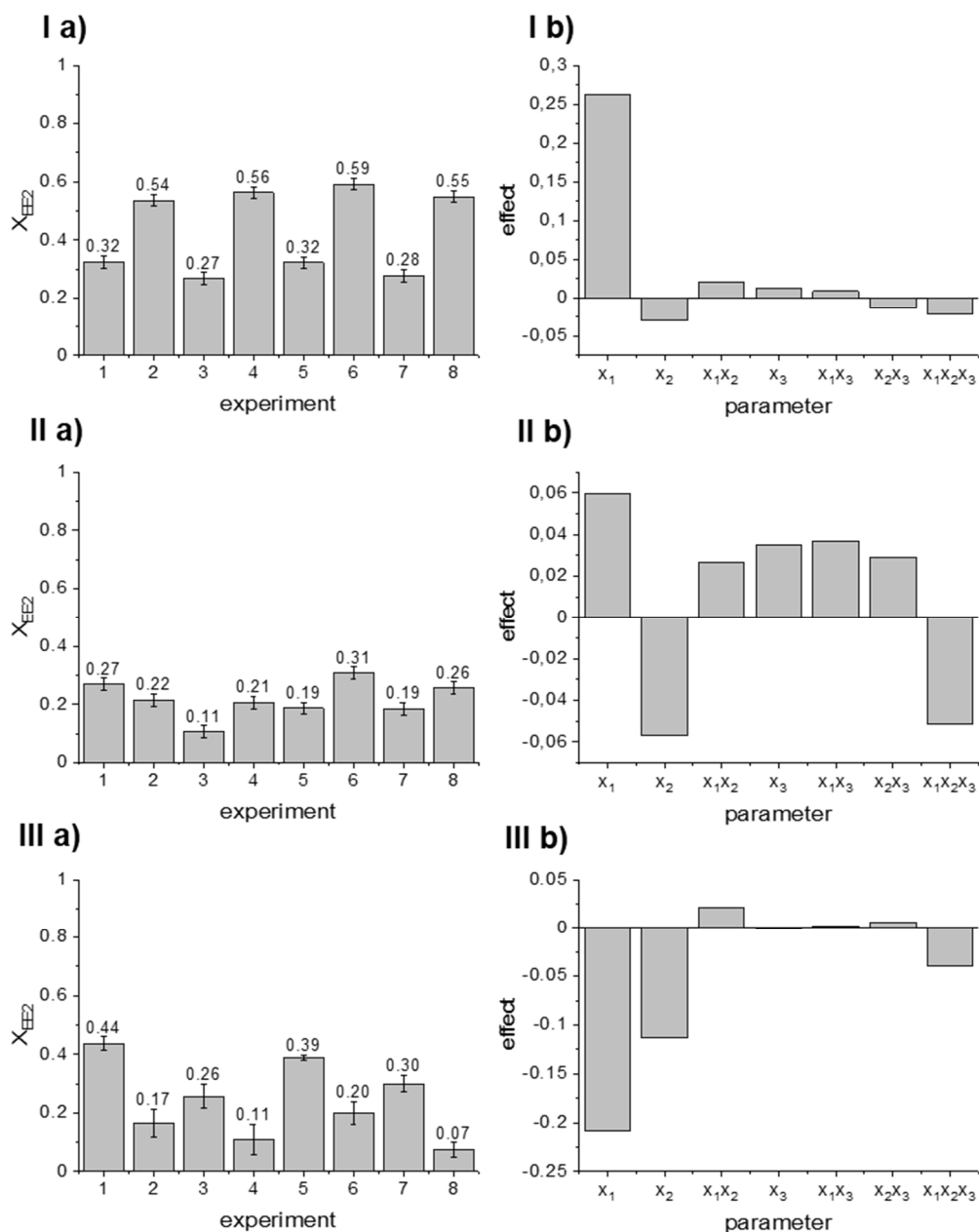


Figure 8. Optimization of the microgap reactor parameters catalyst mass (related to the catalyst bed thickness), solution film thickness and irradiance with combinatorial experiment designs; (I) x_1 : residence time τ : $\tau_- = 0.5$ min, $\tau_+ = 2.0$ min; x_2 : average catalyst layer thickness $d_{avg.}$: $d_{avg,-} = 100.10 \pm 9.13 \mu\text{m}$ ($m_{P25,-} = 0.85 \text{ g}$), $d_{avg,+} = 149.70 \pm 11.94 \mu\text{m}$ ($m_{P25,+} = 1.21 \text{ g}$); x_3 : Irradiance E: $E_- = 362.5 \text{ mW cm}^{-2}$, $E_+ = 1087.5 \text{ mW cm}^{-2}$; block 1: exp. 1, 2, 5, 6, block 2: exp. 2, 3, 7, 8; (II) x_1 : residence time τ : $\tau_- = 0.5$ min, $\tau_+ = 1.0$ min; x_2 : average catalyst layer thickness $d_{avg.}$: $d_{avg,-} = 6.14 \pm 1.96 \mu\text{m}$ ($m_{P25,-} = 100 \text{ mg}$), $d_{avg,+} = 23.14 \pm 2.35 \mu\text{m}$ ($m_{P25,+} = 310 \text{ mg}$); x_3 : Irradiance E: $E_- = 362.5 \text{ mW cm}^{-2}$, $E_+ = 1087.5 \text{ mW cm}^{-2}$; block 1: exp. 1, 2, 5, 6, block 2: exp. 2, 3, 7, 8; (III) x_1 : catalyst mass m_{P25} : $m_{P25,-} = 50 \text{ mg}$ ($d_{avg,-}$ n.d., OOR), $m_{P25,+} = 150 \text{ mg}$ ($d_{avg,+} = 3.86 \pm 1.19 \mu\text{m}$); x_2 : microgap width d_{film} : $d_{film,-} = 250 \mu\text{m}$, $d_{film,+} = 500 \mu\text{m}$; x_3 : Irradiance E: $E_- = 362.5 \text{ mW cm}^{-2}$, $E_+ = 1087.5 \text{ mW cm}^{-2}$, block 1: exp. 1, 3, 5, 7, block 2: exp. 2, 4, 6, 8. For all experiments, the EE2 concentration ($c_{EE2} = 4.5 \text{ mg L}^{-1}$), temperature ($\vartheta = 20^\circ\text{C}$), pH value ($\text{pH} = 7$) and oxygen concentration ($c(\text{O}_2) \approx 8.0 \text{ mg L}^{-1}$) remained constant. For experiment design (III), the modified residence time ($\tau_{mod} = 20 \text{ g min L}^{-1}$) remained constant.

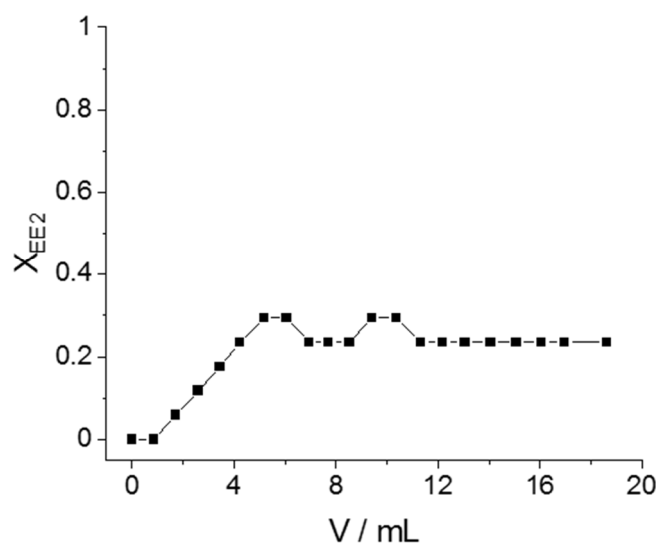


Figure 9. Investigation of the microgap reactor start up behavior; reactant: EE2 (17 α -ethynil estradiol), $c_{\text{start}} = 14.5 \mu\text{g L}^{-1}$, catalyst: P25 immobilized by spray coating on a steel substrate [X6CrNiMoTi17-12-2], calcination: $t = 2 \text{ h}$, $\vartheta = 500^\circ\text{C}$, $m = 90 \text{ mg}$; reaction: $\tau_{\text{mod}} = 30 \text{ g min L}^{-1}$, $E = 362.5 \text{ mW cm}^{-2}$, $\lambda = 365 \text{ nm}$; EE2 content determination by UHPLC-MS/MS.

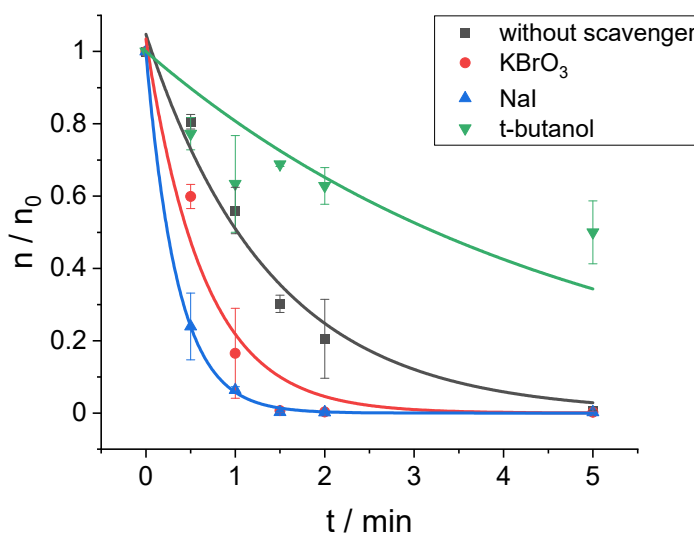
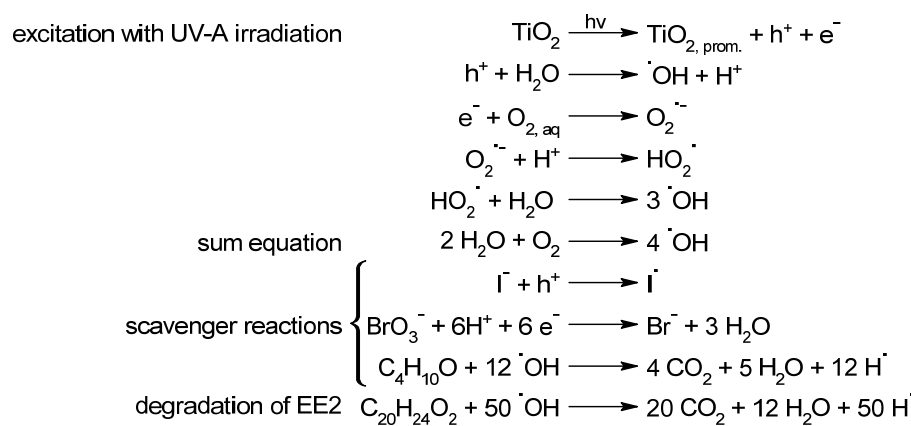


Figure 10. Reaction monitoring of the photocatalytic degradation of EE2 (17 α -ethynil estradiol) and investigation of the influence of scavenger substances on the degradation kinetics. The experiment was carried out with a 60-fold parallel stirring UV-A LED photoreactor system [29], in which each value resembles a separate catalytic experiment, with triple determination; $V_{\text{EE2-solution}} = 5 \text{ mL}$, $c = 4.5 \text{ mg L}^{-1}$; scavenger additives: NaI, KBrO₃, t-butanol, $c_{\text{scavenger}} = 3 \text{ mmol L}^{-1}$; reaction parameters: catalyst P25 (calcined), $m_{\text{P25}} = 7.5 \text{ mg}$, $f_{\text{rot}} = 800 \text{ min}^{-1}$, $t_{\text{dark}} = 30 \text{ min}$, $E = 384 \text{ mW cm}^{-2}$, $\lambda = 365 \text{ nm}$; SPE-GC-MS analysis (determination of ion count n as a measure of the amount of substance from the extracted ion current (EIC), precursor ions: $[\text{M}] + 440 \text{ m/z}$, $[\text{M}-15] + 425 \text{ m/z}$; $k(\text{without scavenger}) = 0.012 \text{ s}^{-1}$, $k(\text{KBrO}_3) = 0.026 \text{ s}^{-1}$, $k(\text{NaI}) = 0.048 \text{ s}^{-1}$, $k(\text{t-butanol}) = 0.004 \text{ s}^{-1}$.



Scheme 1. Assuming the complete mineralization of EE2 to carbon dioxide [30–32].

2.6. Influence of Doping Metals

The influence of copper-doping of P25 was investigated in screening experiments utilizing a 60-fold parallel stirring UV-A LED photoreactor [29]. The use of different copper-doping degrees indicated that the conversion of EE2 was amplified by small dosages of copper; in fact, conversion approximately tripled compared to undoped, calcined P25 (Figure 12). With the aim of transferring this coherence to the microgap reactor, two different preparation techniques were considered. First, P25 was impregnated with a copper-containing solution before coating the steel substrate; second, an already immobilized P25 layer was impregnated. Both experiments were performed with same amount of copper ($x_{\text{Cu}} = n_{\text{Cu}} n_{\text{Ti}}^{-1} \approx 2\%$), and were tested at different modified residence times ($\tau_{\text{mod}} = 10, 20, 30, 50, 70, 100 \text{ g min L}^{-1}$). The results depicted in Figure 12 show that the conversion amplifying effect of copper-doping could be partly preserved in the microgap reactor (see Figure 13), no matter how the doping copper had been introduced to the P25, while the specimen doped before spray coating showed slightly higher activity. Roughly a 29% increase in conversion was found compared to the undoped, calcined P25.

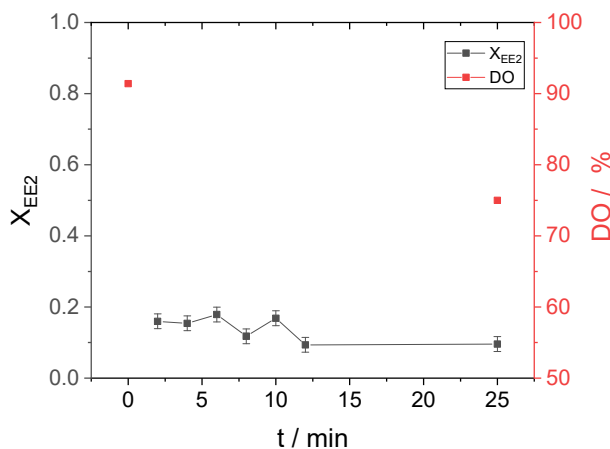


Figure 11. Dissolved oxygen consumption determination during a continuous photocatalytic micro-gap reactor experiment. A large volume ($V = 20 \text{ mL}$) of irradiated reactant solution was collected in an equilibrated state of conversion ($t = 12\text{--}24 \text{ min}$); reactant: EE2 (17α -ethinyl estradiol), $c_{\text{start}} = 15 \mu\text{M}$ in pure water; catalyst: P25 (immobilized by spray coating on steel substrate [X6CrNiMoTi17-12-2], calcined, $\vartheta = 500^\circ\text{C}$, $t = 2 \text{ h}$), $d_{\text{avg.}} = 6.90 \pm 3.65 \mu\text{m}$; reaction: $\tau_{\text{mod}} = 6.6 \text{ g min L}^{-1}$, $E = 362.5 \text{ mW cm}^{-2}$, $\lambda = 365 \text{ nm}$; conversion analysis: GC-MS (EIC: $[M] + 440 \text{ m/z}$, $[M-15] + 425 \text{ m/z}$), process standard deviation is given; dissolved oxygen (DO): before irradiation DO = 91.4%, $c(\text{O}_2) = 8.26 \text{ mg L}^{-1}$, $\vartheta = 20.3^\circ\text{C}$, after irradiation DO = 75.0%, $c(\text{O}_2) = 6.48 \text{ mg L}^{-1}$, $\vartheta = 22.7^\circ\text{C}$.

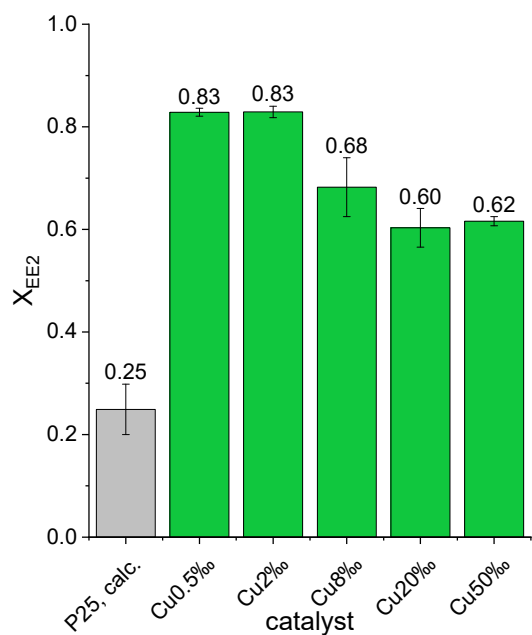


Figure 12. Screening of copper-doped P25 catalysts with different doping degrees. The experiment was carried out with a 60-fold parallel stirring UV-A LED photoreactor system [29]. Each value resembles a separate catalytic experiment, triple determination; reactant: EE2 (17 α -ethinyl estradiol), $V = 5 \text{ mL}$, $c_{\text{start}} = 4.5 \text{ mg L}^{-1}$; catalysts: P25, calcination: $t = 2 \text{ h}$, $\vartheta = 500 \text{ }^\circ\text{C}$, $m_{P25} = 7.5 \text{ mg}$; CuX \% , P25 catalyst impregnated with copper acetate solution in pure water ($c(\text{Cu(OAc)}_2) = 8.6 \text{ mmol L}^{-1}$, $x_{\text{Cu}} = n_{\text{Cu}} n_{\text{Ti}}^{-1} = 0.5, 2, 8, 20, 50 \text{\%}$), calcination: $t = 2 \text{ h}$, $\vartheta = 500 \text{ }^\circ\text{C}$; reaction: $f_{\text{rot}} = 800 \text{ min}^{-1}$, $t_{\text{dark}} = 30 \text{ min}$, $t_{\text{irradiation}} = 1.5 \text{ min}$, $E = 384 \text{ mW cm}^{-2}$, $\lambda = 365 \text{ nm}$; EE2 content determination by SPE-GC-MS analysis (determination of ion count n as measure for the amount of substance from the extracted ion current (EIC), precursor ions: $[\text{M}] + 440 \text{ m/z}$, $[\text{M}-15] + 425 \text{ m/z}$).

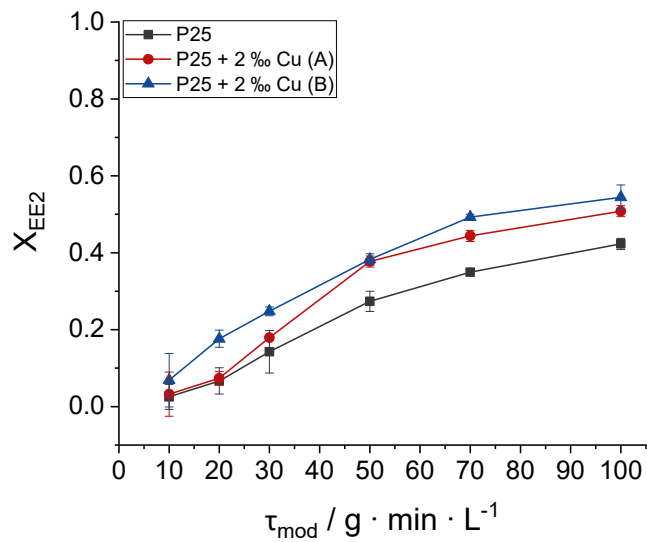


Figure 13. Investigation of the influence of copper-doping after immobilization by spray coating, triple determination. Experiments were carried out in the microgap reactor; reactant: EE2 (17 α -ethinyl estradiol), $c_{\text{start}} = 14.5 \text{ }\mu\text{g L}^{-1}$; catalysts: P25, immobilized by spray coating on a steel substrate [X6CrNiMoTi17-12-2], calcination: $t = 2 \text{ h}$, $\vartheta = 500 \text{ }^\circ\text{C}$, $m = 90 \text{ mg}$; P25 + 2% Cu, immobilized P25 catalyst impregnated with copper acetate solution ($c(\text{Cu(OAc)}_2) = 8.32 \text{ g L}^{-1}$, $m = 0.07 \text{ g}$, $x_{\text{Cu}} = n_{\text{Cu}} n_{\text{Ti}}^{-1} \approx 2 \text{\%}$), A: impregnation before spray coating, B: impregnation after spray coating; reaction: microgap reactor, $E = 362.5 \text{ mW cm}^{-2}$, $\lambda = 365 \text{ nm}$; analysis: EE2 content determination by UHPLC-MS/MS.

3. Discussion

A novel microgap reactor concept for the photocatalytic degradation of micropollutants in aqueous solution with a titanium dioxide catalyst immobilized by spray coating was investigated. The utilization of a combinatorial experiment design made it possible to examine the influence of multiple parameters, such as the solution film thickness in the reactor, the P25-based catalyst layer thickness and irradiance in a single experiment on the conversion of EE2. This approach emphasizes factor effect determination, as well as the calculation of interaction effects between the various factors. In general, thinner liquid film and catalyst layers were found to favor the degradation of EE2. This coherence can be explained by the fact that low diffusion coefficients in liquids cause low mobilities of active species in the solution. Based on the obtained results, it may be concluded that this coherence significantly influences the conversion of EE2. It was found that EE2 is degraded by hydroxyl radicals in the solution film, but not on the surface of the catalyst, as EE2 is not a surface-active molecule, and therefore, does not become enriched on the catalyst surface, where excitons are formed by irradiation. Therefore, the formed excitons reacted with the surrounding water, forming hydroxyl radicals. Consequently, these active species had to diffuse out of the porous catalyst bed into the solution bulk to degrade the pollutant, since the pollutant molecule had no affinity toward the catalyst. Due to the short lifespan of hydroxyl radicals [33], this process is of low probability and only applies to the solution which is directly in contact with, or very close to, the catalyst, with the rest of the solution passing by unaffected. In order to address this problem, the microgap was made as thin as possible (i.e., $d_{\text{microgap}} = 250 \mu\text{m}$), resulting in a larger solution film thickness ($d_{\text{film}} = 490 \mu\text{m}$, $d_{\text{avg.,catalyst layer}} = 10 \mu\text{m}$) in the irradiated area due to the nature of the construction of the reactor. Utilizing thinner microgaps ($d_{\text{microgap}} = 100 \mu\text{m}$) was not possible because of leakage problems. In this context, the results showed that thinner catalyst layers positively influenced EE2 degradation, presumably for the same reasons. Struggling with low diffusion coefficients, the active hydroxyl radicals were not able to diffuse from a thick catalyst bed ($d_{\text{avg.,catalyst bed}} > 100 \mu\text{m}$), due to recombination within the layer, resulting in a strong mass transport limitation and low catalyst efficiency for photocatalytic degradation (compare Figure 8I). Consequently, the same correlation was observed as discussed above, i.e., only EE2 molecules close to the catalyst surface in the porous bed were degraded while the solution bulk was unaffected, making the photocatalytic degradation process highly inefficient. The optimal catalyst layer thickness was found to be close to $d_{\text{avg.,catalyst layer}} \approx 10 \mu\text{m}$, $m_{\text{P25}} \approx 100 \text{ mg}$. With regard to the doped titanium dioxide catalyst, an advantage in EE2 conversion was found with small amounts of added copper ($x_{\text{Cu}} = n_{\text{Cu}} n_{\text{Ti}}^{-1} \approx 2\%$). With the addition of copper in oxidation state +2, unoccupied valence orbitals were introduced into the material, which could then presumably function as electron scavengers, stabilizing excitons by separating electron-hole pairs. This coherence favored the formation of hydroxyl-radicals, which improved the conversion of EE2. Regarding the observed conversions ($X_{\text{EE2}} = 0.65$, $\tau_{\text{mod}} = 100 \text{ g min L}^{-1}$, $\tau = 2.7 \text{ min}$, copper-doped P25, $x_{\text{Cu}} = n_{\text{Cu}} n_{\text{Ti}}^{-1} \approx 2\%$), the described technique with residence times actually in the minute range may represent a valuable addition to wastewater treatment technology, in which collected water is processed in a matter of days. The scaling up of dedicated microgap reactors for wastewater treatment plants will be significant challenge; such facilities deal with a daily income of thousands of cubic meters of water, which would require vast surfaces of thin films. In this regard, reactor designs with stackable units could be a favorable solution.

4. Materials and Methods

4.1. Materials

4.1.1. Chemicals

For the photocatalytic experiments, a 17 α -ethinyl estradiol stock solution (EE2, $c_{\text{EE2}} = 4.5 \text{ mg L}^{-1}$, Sigma-Aldrich, Taufkirchen, Germany) was prepared in pure water (PURELAB flex 3, ELGA LabWater Systems, Celle, Germany R = 18.2 M Ω , TOC = 1 ppb). This solution was later further diluted as required. The preparation of immobilized catalyst

layers was carried out with a P25 (nanoparticulate TiO_2 , AEROXIDE[®], Evonik Industries, Mönchengladbach, Germany) disperser containing a titania sol (TiSol-NH₄, NYACOL Nano Technologies, Ashland, Massachusetts, containing 10 wt.% TiO_2 (nanoparticulate), carrier: water) which also functioned as a binder, as well as ethylene glycol (VWR, Darmstadt, Germany, Analar NORMAPURE) which served as a high boiler. For impregnation purposes, an aqueous copper acetate solution in pure water (Supleco, Bellefonte, Pennsylvania, EMPLURA[®]) was utilized. Scavenger substances such as sodium iodide (Roth, Karlsruhe, Deutschland, >99%), potassium bromate (VEB Laborchemie APOLDA, Apolda, Germany, for analysis) and tertiary butanol (Merck, Taufkirchen, Germany, for analysis) were utilized in the screening experiments. The GC-MS analyses were prepared with the help of acetone (SupraSolv[®], Sigma-Aldrich, Taufkirchen, Germany), and derivatization was carried out in *N,N*-dimethylformamide (SupraSolv[®], Sigma-Aldrich, Taufkirchen, Germany) by *N*-methyl-*N*-(trimethylsilyl)trifluoroacetamide (MSTFA, Sigma-Aldrich, Taufkirchen, Germany). In addition, chrysene-d₁₂ ($c = 0.1 \text{ g L}^{-1}$ in acetone, Supleco[®], Sigma-Aldrich, Taufkirchen, Germany) was deployed as an internal standard. Helium (Alphagaz, Düsseldorf, Germany, 99.999%) was used as the GC carrier gas. For the UHPLC-MS/MS analysis, acetonitrile (Merck, Taufkirchen, Germany, Supelco[®], hyper grade for LC-MS) and pure water were used as mobile phases, both containing trace amounts of ammonium fluoride ($c = 0.4 \text{ mg L}^{-1}$, Merck, Taufkirchen, Germany, Supelco[®], analytical grade). Argon (Alphagaz, Düsseldorf, Germany, 99.9999%) was used as the collision gas for the MRM (multireaction monitoring) experiments. All chemicals were used as received and without further purification.

4.1.2. Photocatalysis Microgap Reactor

The microgap reactor consisted primarily of six parts: the bottom and the cover plate (length: 35.0 cm, width: 17.5 cm, height: 1.5 cm, steel type X6CrNiMoTi17-12-2), a UV irradiation transparent fused silica window (length and width: 14.5 cm, height: 1.0 cm), a gap width (d_{microgap}) determining PTFE foil (High-tech-flon[®], Konstanz, Germany, length: 35.0 cm, width: 17.5 cm, height: 250–500 μm) and an air cooled UV-A LED array (Opsytech Dr. Gröbel GmbH, Ettlingen, Germany, UV-LED Series L S, emitting area: length: 10 cm, width: 5 cm, $\lambda = 365 \text{ nm}$, $E_{\text{max}} = 1450 \text{ mW cm}^{-2}$) connected to its controller (Opsytech Dr. Gröbel GmbH, Ettlingen, Germany, LED-Control S) mounting the reactor. A massive stainless-steel plate (type: X6CrNiMoTi17-12-2, length: 10 cm, width: 5 cm, height: 0.5 cm) with round edges was utilized as a substrate. Into this substrate, a recess was milled in the bottom plate (depth: 0.525 cm), leaving a certain height ($d_{\text{catalyst,max}} = 250 \mu\text{m}$) above it relative to the upper surface of the bottom plate for the catalyst layers. This gave us a reasonable reaction volume in the irradiation area, depending on the catalyst layer thickness ($V_{\text{min}} = 1.25 \text{ mL}$ (estimations: $d_{\text{catalyst}} = d_{\text{film}} = 250 \mu\text{m}$), $V_{\text{max}} = 3.75 \text{ mL}$ (estimations: no catalyst, $d_{\text{film}} = 500 \mu\text{m}$)). Regarding this coherence, the modified residence time τ_{mod} was used to compare different catalysts in order to compensate for the various catalyst layer thicknesses, and thus, reactor volumes. The reactor setup was fixed by eighteen screws (BETEC Befestigungstechnik GmbH, Chemnitz, Germany socket head cap screws with inner decant, DIN 912 A2, M6) and placed upon a heat exchanger, which was connected serially to a tempering cup (KGW Isotherm, Karlsruhe, Germany, type T-GL 2000, $V = 2 \text{ L}$) and finally to a thermostat (Julabo, Seelbach, Germany, F12), thereby keeping the reactant stock solution inside the cup at a set temperature via the heat exchanger. Inside the cup, a glass frit with a glass tube was connected to a piece of PTFE tubing, which made it possible to introduce gases like compressed air to the solution stock. Additionally, the cup was locked onto a magnetic stirrer for equilibration purposes. A peristaltic pump (LAMBDA, Brno, Czech Republic, MAXIFLOW) holding a silicone tube (VWR, Darmstadt, Germany, inner diameter: 4 mm, outer diameter: 6 mm) allowed the reactant solution to flow from the stock through the reactor system. Special PTFE fittings (Reichelt Chemietechnik, Heidelberg, Germany, MULTIFIT[®]-EMP-3, inner diameter: 4 mm, outer diameter: 6 mm, external threads: M5) and their corresponding screw holes in the bottom plate made it possible to connect the

tubing from the peristaltic pump to one side the reactor and, more importantly, to the silicone outlet tubing on the opposite site. Different glass containers were used to collect the dispensed liquids from the outlet tubing. For as illustration of the described system, see Figure 14. For a detailed view of the microgap reactor, consult Figure 17.

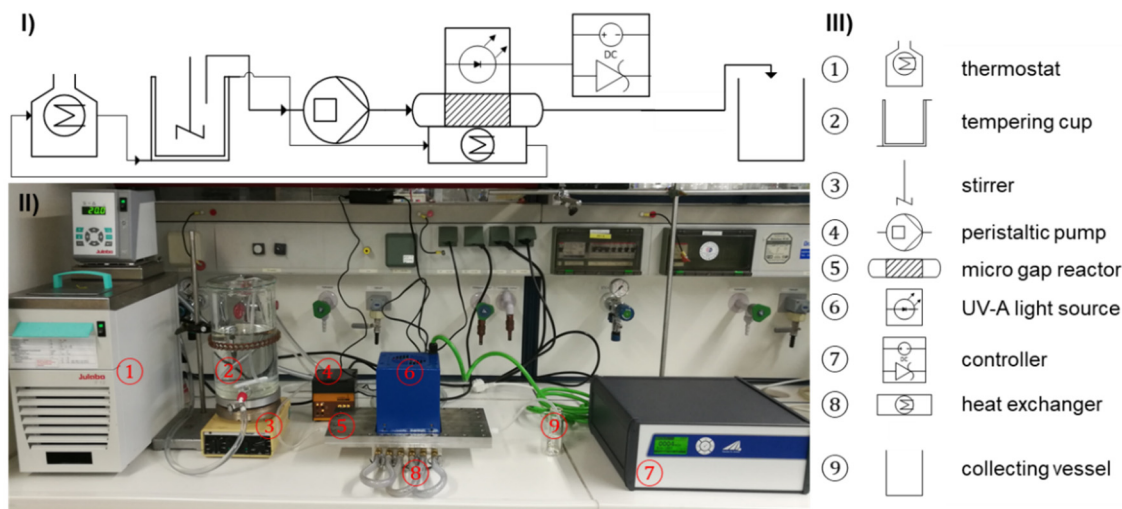


Figure 14. Overview of the microgap experimentation set up; (I) process flow diagram, (II) photograph of process implementation, (III) legend; glass frit for gas inlet not shown.

4.2. Methods

4.2.1. Catalyst Preparation

Since it was not possible to process the nanoparticulate P25 as received in a robust catalyst layer using the spray coating process, the titanium dioxide powder had to be dispersed in excess pure water and then calcined (Carbolite, Neuhausen, Germany, AAF110, $\vartheta = 500\text{ }^{\circ}\text{C}$, $t = 2\text{ h}$) before use. The colorless solid obtained by this procedure was manually pounded in an agate mortar and sifted ($d < 100\text{ }\mu\text{m}$) to obtain a catalyst powder ($d_{10} = 5.63 \pm 0.32\text{ }\mu\text{m}$, $d_{50} = 34.11 \pm 0.311\text{ }\mu\text{m}$, $d_{90} = 75.50 \pm 1.80\text{ }\mu\text{m}$, particle size distribution [compare Section 4.2.4], medium: water) which was fine enough to pass through the spray gun outlet. In addition, oxidic copper impregnated P25 catalysts were produced with different amounts of copper ($x_{\text{Cu}} = 0.5, 2, 8, 20, 50\%$; $x_{\text{Cu}} = n_{\text{Cu}} n_{\text{Ti}}^{-1}$) as follows. First, a certain amount of P25 ($m_{\text{P25}} = 1.2\text{ g}$) was weighed in PTFE cups and combined with a doping degree defining amount of copper acetate solution ($c(\text{Cu(OAc)}_2) = 8.6\text{ mmol L}^{-1}$ in pure water). The cups were then filled with excess water and placed into an aluminum jacket mounted on a heatable vortexer ($\vartheta = 80\text{ }^{\circ}\text{C}$, $f = 200\text{ min}^{-1}$) for homogenization purposes. The process continued even after the solvent had evaporated to dryness ($t = 24\text{ h}$). The obtained mint green pills were pounded, calcined, pounded again and then sifted, as described above.

4.2.2. Substrate Preparation

For the immobilization of the catalysts on a steel substrate, the spray coating technique was chosen. Before the coating process could take place, the substrate surface was sandblasted (quartz, $d_{\text{avg,quartz}} = 20\text{ }\mu\text{m}$, $p = 500\text{ kPa}$) to increase its roughness (Hommel-Etamic T8000, Jenoptik, Jena, Germany, probe type: TKU300, $R_z = 36.37 \pm 2.02\text{ }\mu\text{m}$, $R_a = 5.43 \pm 0.22\text{ }\mu\text{m}$). This enhanced the adhesion of the catalyst suspensions. Further treatments did not influence the surface roughness. The obtained plates were brushed, rinsed with water, dried and then immersed in ethyl acetate in an ultrasonic bath ($t = 15\text{ min}$). After drying, they were treated with ozone (PSD-UV4, Novascan Technologies, Ames, Iowa, $t = 30\text{ min}$) to remove leftover organics from the surface.

4.2.3. Catalyst Layer Preparation

Before undertaking the coating process, a suspension containing calcined P25 ($m = 150 \text{ mg}$), the titania sol binder ($V = 1 \text{ mL}$) and ethylene glycol ($V = 50 \mu\text{L}$) was magnetically stirred ($t = 24 \text{ h}$, $f_{\text{rot}} = 300 \text{ min}^{-1}$). The freshly prepared suspension was transferred into a HVLP spray gun (HVLP—high velocity low pressure; HS-25 HVLP HV3, Krautzberger GmbH, Eltville am Rhein, Germany) and manually sprayed ($v_t \approx 0.2 \text{ m s}^{-1}$, $p = 100 \text{ kPa}$) on the substrate, which was positioned on a heating plate ($\vartheta = 90^\circ\text{C}$). Aiming to cover the whole substrate surface uniformly, application was carried out by maintaining the spray gun—facing the outlet downward toward the substrate surface—at a certain distance ($h = 15 \text{ cm}$), pulling the trigger before the ejected spray cone could hit the edge of the plate and releasing it after the spray cone had left the edge at the opposite site of the substrate (Figure 15). Since the spray cone did not open wide enough to cover the whole surface at once, the steel plate was segmented into three parts. These were coated by sequentially alternating the movement direction for each section, as indicated in Figure 16. This process was repeated until the entirety of the prepared suspension had been ejected. Afterwards, the substrate with the soft catalyst layer was carefully transferred to the calcination furnace ($\vartheta_{\text{init}} = 25^\circ\text{C}$, ramp: 1 K min^{-1} , $\vartheta_{\text{max}} = 500^\circ\text{C}$, $t_{500^\circ\text{C}} = 2 \text{ h}$). After calcination, a colorless solid catalyst layer was obtained. With the aim of introducing doping elements to the catalyst, the already calcined catalyst layer was impregnated as described above with transition metal salt solutions e.g., copper acetate ($c(\text{Cu(OAc)}_2) = 8.32 \text{ g L}^{-1}$), in pure water. Using this technique, the doping degree could easily be varied and determined by measuring the mass of the solution sprayed onto the catalyst bed. As such, the substrate was not heated at this time. The impregnated catalyst bed was subsequently calcined applying the same parameters.

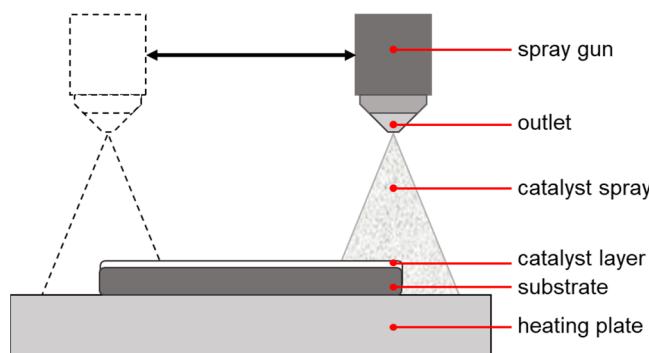


Figure 15. Schematic sideview of the spray coating process; arrow indicates the direction of movement.



Figure 16. Schematic top view of the substrate deployed for catalyst immobilization, divided into three parts (I, II, III). Where the spray cone ejected by the spray gun was centered for each stride, arrows indicate the starting points of the strides (1–6); the whole coating process required more than the six indicated strides.

4.2.4. Catalyst Characterization

The synthesized catalysts were characterized by powder X-ray diffraction with an automated, multipurpose x-ray diffractometer (Rigaku, Tokyo, Japan SmartLab, Cu anode, D/tex Ultra250 detector, graphite monochromator) and Brunauer-Emmett-Teller gas ph-

ysisorption measurements (BET; NOVAtouch 4LX, Quantachrome Instruments, Boynton Beach, Florida; adsorbate: nitrogen; pore size according to Dollimore-Heal). Concerning the catalyst layer thickness, an eddy current method was utilized (Fischer, Sindelfingen, Germany, Fischerscope® MMS®, probe: ETA 3.3–3.5). The particle size distribution was determined by a static light scattering method (CILAS, Orléans, France 930, particle size analyzer). The surface structure was investigated by environmental scanning electron microscopy (ESEM, Carl Zeiss Microscopy GmbH, Jena, Germany, REM Zeiss EVO15).

4.2.5. Screening Experiments

The influence of scavenger substances and copper doping was investigated utilizing a self-constructed, 60-fold parallel stirring, UV-A LED photoreactor in screening experiments, as described in detail in a prior publication [29]. Sodium iodide, potassium bromate, and tertiary butanol were utilized as scavengers ($c_{\text{scavenger}} = 3 \text{ mmol L}^{-1}$), according to the method described by Abramović [30]. An aliquot proportion of tertiary butanol was directly added to the reaction suspension, while sodium iodide and potassium bromate were dissolved in pure water ($c = 150 \text{ mmol L}^{-1}$) prior to their addition. The pH value remained constant ($\text{pH} = 7$) for all reactions. The EE2 conversion for each sample was determined by GC-MS analysis.

4.2.6. Photocatalytic Experiments

The photocatalysis microgap reactor was assembled as follows. First, the whole bottom plate (Figure 17I) was wetted with pure water to enable air bubble-free construction. Next, the coated steel substrate was inserted into the water-filled milling in the bottom plate. Afterwards, the gap width determining PTFE foil (Figure 17II) was placed on top of the bottom plate; the top of the foil was then wetted again with pure water before being covered with the glass window holding top plate. Finally, the reactor was secured in this configuration using screws (Figure 17III). An estrogen solution was prepared by diluting the targeted amount of EE2 stock solution in pure water. Aiming for oxygen saturation in the prepared solution, pressured air was introduced ($p = 0.2 \text{ bar}$, $t = 60 \text{ min}$). The dissolved oxygen levels in the tempering cup were monitored by *in situ* fluorescent quenching measurements (VWR, Darmstadt, Germany, DO 220 M) to check the constancy. To remove any remaining air bubbles, the reactor was flushed with pure water ($V = 1 \text{ L}$), and subsequently, with estrogen solution ($V = 0.1 \text{ L}$), which was discarded. At this point, the whole reactor system was flooded with estrogen solution. To gain an equilibrated state, the solution was circulated ($V = 0.6 \text{ L}$) through the system. After this conditioning routine, the UV-A LED array was mounted on to the glass window and connected to a controller and energy source. Different photocatalytic experiments were performed by the setting flow rate, pump time, irradiation intensity and irradiation time, and then starting the pump and light source at the same time. Since the reactor contained a dead volume after the active irradiated part (Figure 17II), the initial pumped volume ($V = 10 \text{ mL}$, see Results: Start-up behavior) was discarded and a subsequent volume was collected for analysis. The EE2 conversion determination was ensued by UHPLC-MS/MS analyses.

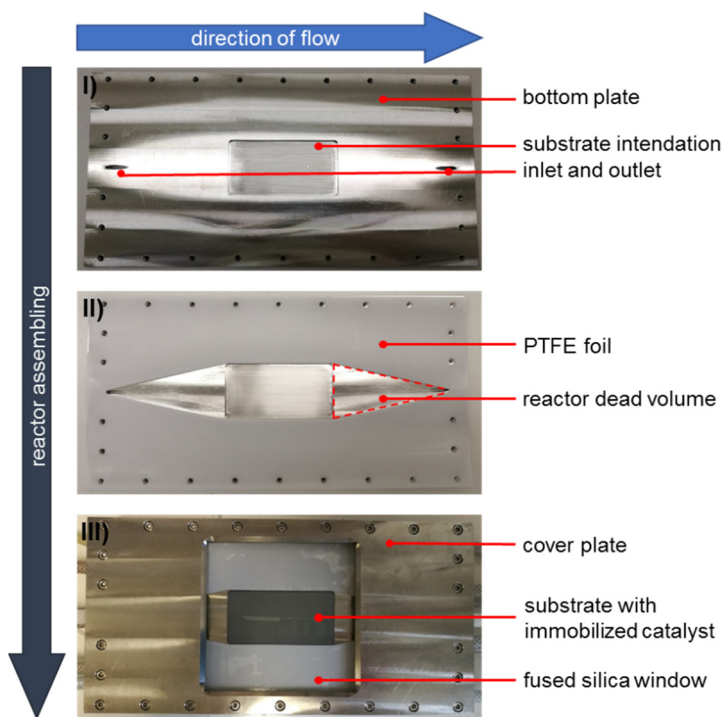


Figure 17. Overview of microgap reactor assembling. The described reactor dead volume (II) adds to the outlet connected tubing (not shown) to $V_{\text{dead-volume}} \approx 4 \text{ mL}$.

4.2.7. GC-MS Analysis

A gas chromatograph coupled to a mass spectrometer (GC-MS) was deployed to evaluate the conversion of samples derived from the screening and combinatorial experiments. These samples typically featured a high EE2 concentration ($c_{\text{max}} = 4.5 \text{ mg L}^{-1}$). A slightly modified GC-MS analysis protocol, according to a prior publication [29], was applied. Briefly, the samples were diluted after derivatization ($V = 400 \mu\text{L}$, solvent: DMF), the injection volume was decreased ($V = 1 \mu\text{L}$), and a solvent plug injection method was utilized. Thus, linearity of calibration could be preserved.

4.2.8. UHPLC-MS/MS Analysis

Later in the investigation process, an ultrahigh performance liquid chromatograph (UHPLC, ACQUITY UPLC H-Class, Waters Cooperation, Milford, Massachusetts) with a tandem mass spectrometer (MS/MS, Xevo TQ-XS, Waters Cooperation, Milford, Massachusetts) coupling, equipped with a special electron spray ion source (UniSprayTM, Waters Cooperation, Milford, Massachusetts), became available and made it possible to examine samples natively without further preparation, as is the case with GC-MS analysis, where a derivatization of the analyte molecules is necessary. It turned out that the obligatory derivatization process for GC-MS was not able to transfer all analyte molecules quantitatively into their derivatives at low EE2 concentrations. Thus, UHPLC-MS/MS was utilized for quantification purposes for the samples derived from catalyst doping and matrix effect determination of the microgap reactor with low analyte concentration ($c_{\text{max}} = 150 \mu\text{g L}^{-1}$). Concerning the UHPLC, a packed column (ACQUITY UPLC BEH C18, particle size: $1.7 \mu\text{m}$, width: 3.0 mm , length: 100 mm , Waters Cooperation) was set up. Concerning the analysis protocol, a sample ($V = 1 \mu\text{L}$) was drawn from a vial (VWR, $V_{\text{capacity}} = 1.5 \text{ mL}$, diameter: 11.6 mm , height: 32 mm) sealed with a PTFE septum screw cap by the autosampler. This was then injected into the sample loop, from where the analytes were transported to the column by the mobile phase stream ($Q = 0.6 \text{ mL min}^{-1}$; initial gradient: 70: 30/A: B, $t_{3.50 \text{ min}} = 5$: 95/A: B, $t_{5.60 \text{ min}} = 70$: 30/A: B; run time: 8.60 min), and subsequently, to the MS/MS. Here, MRM experiments (MRM—multireaction monitoring, negative ionization mode, capillary voltage: 2.00 kV , cone gas flow: 150 L h^{-1}

of N₂ [nitrogen generator, cmc Instruments, NGM 11], desolvation temperature: 600 °C, desolvation gas flow: 1200 L h⁻¹ of N₂, nebulizer pressure: 5.5 bar) were performed for qualification and, more importantly, quantification purposes. See Table 3 for quantifier and qualifier ion information.

Table 3. Multireaction monitoring ion transitions utilized for qualification and quantification, $\frac{m}{z}$ —mass-to-charge ratio.

Analyte	$\frac{m}{z}$ of Transitions	Cone Voltage/V	Collision Energy/eV
17 α-ethinyl estradiol	295.10 > 143.00	40	47
	295.10 > 145.00	40	36
	295.10 > 159.00	40	34

4.2.9. Combinatorial Design

With the objective of finding the optimal reaction parameters, especially regarding the variable conversion of EE2, X_{EE2}, an orthogonal full-factorial design with two levels of three variables (23) as well as blocking was utilized. Blocking was necessary, since the reactor had to be disassembled to exchange the substrate. The parameters catalyst mass m_{P25}, irradiance E, residence time τ and reactor gap width d_{film} were under investigation. At the same time, the temperature θ, the oxygen content c(O₂) of the stock solution, its pH value and its EE2 concentration c_{EE2} remained constant throughout the combinatorial experiments; see Table 4 for the experimental plan. The obtained information regarding the objective variable was mathematically processed by a statistical equation [34] (Equation (3)) in order to obtain the effect of a specific variable x₁, x₂, x₃, deploying factor p (− or +) and the dependent value of the objective variable Z alongside the total number of experiments n.

$$\text{effect}(i) = \frac{\sum_{j=1}^n p_{ij} Z_j}{0.5n} \quad (3)$$

Table 4. Experimental plan of a 2³ full-factorial combinatorial design; x₁, x₂, x₃ indicate variables x_j of interest; +, − are the coded variables p_{ij} at high level (+1) or at low level (−1); Z_j objective variable.

Experiment	x ₁	x ₂	x ₃
1	−	−	−
2	+	−	−
3	−	+	−
4	+	+	−
5	−	−	+
6	+	−	+
7	−	+	+
8	+	+	+

5. Conclusions

The presented microgap reactor concept, utilizing thin catalyst layers immobilized by spray coating, represents a highly functional method for the degradation of 17 α-ethinyl estradiol (EE2) from continuously flowing aqueous solutions (X_{EE2} = 0.65 in t = 2.7 min). The activity of the commercially available photocatalytic standard catalyst P25 (nanoparticulate titanium dioxide) was amplified by a factor of almost three by impregnation with small amounts of copper (x_{Cu} = n_{Cu} n_{Ti}⁻¹ ≈ 2%). Therefore, the reactor design described in this report may constitute a valuable improvement to photocatalysis reactor technology. The utilized steady flow conditions, alongside declined mass transport limitation, the deployment of energy efficient LED light source technologies and commercially available catalysts, elevate this reactor concept to a promising technology for future developments in wastewater treatment. Prospective works should focus on the investigation of reactions of other containments, as well as matrix effects.

Author Contributions: T.B.E. designed and built the experimental setups, conducted experiments and analyses, evaluated the data and wrote this paper, M.Z. constructed the microgap reactor, C.H. conducted scavenger screening experiments, S.S.-S. designed the experimental setups, supervised the work and reviewed the article, T.S. supervised the work, K.S. supervised the work and reviewed the article. All authors have read and agreed to the published version of the manuscript.

Funding: The publication of this article was funded by Chemnitz University of Technology.

Data Availability Statement: Data is contained within the article.

Conflicts of Interest: The authors declare no conflict of interest.

Abbreviations

AOP	advanced oxidation process
BET	Brunauer–Emmett–Teller
c	concentration
cps	counts per second
d	thickness
DIN	Deutsches Institut für Normung
DMF	N, N-dimethyl formamide
DO	dissolved oxygen
E	irradiance
EE2	17 α -ethinyl estradiol
E _g	band gap energy
EIC	extracted ion current
ESEM	environmental scanning electron microscopy
f _{rot}	rotation speed
GC-MS	gas chromatography with mass spectrometry coupling
h	height
I	amperage
IUPAC	International Union of Pure and Applied Chemistry
UHPLC-MS/MS	ultra high performance liquid chromatography with tandem mass spectrometry coupling
LED	Light emitting diode
LOD	limit of detection
LOQ	limit of quantification
m	mass
MRM	multireaction monitoring
MSTFA	N-(trimethylsilyl)trifluoroacetamide
OOR	out of range
P	pressure
ppb	parts per billion
ppm	part per million
PSD	process standard deviation
PTFE	polytetrafluoroethylene
XRD	powder X-ray diffraction
Q	volume flow
R ²	coefficient of determination
R _a	mean roughness, span
R _z	mean roughness, arithmetical mean deviation
SSA	specific surface area
t	time
τ	residence time
TIC	total ion current
TOC	total organic content

U	voltage
UHPLC	ultra high performance liquid chromatography
UV-A	ultraviolet irradiation type A
V	volume
v_f	feed rate
wt.%	weight fraction
x	mole fraction
ϑ	temperature
λ	wavelength
τ_{mod}	modified residence time

References

- Raza, A.; Razzaq, A.; Mahmood, S.S.; Zou, X.; Zhang, X.; Lv, Y.; Xu, J. Impact of Climate Change on Crops Adaptation and Strategies to Tackle Its Outcome: A Review. *Plants* **2019**, *8*, 34. [[CrossRef](#)]
- Hailemariam, K. Impact of climate change on the water resources of Awash River Basin, Ethiopia. *Clim. Res.* **1999**, *12*, 91–96. [[CrossRef](#)]
- Goyal, M.K.; Surampalli, R.Y. Impact of Climate Change on Water Resources in India. *J. Environ. Eng.* **2018**, *144*, 04018054. [[CrossRef](#)]
- Cabral, H.; Fonseca, V.; Sousa, T.; Leal, M.C. Synergistic Effects of Climate Change and Marine Pollution: An Overlooked Interaction in Coastal and Estuarine Areas. *Int. J. Environ. Res. Public Health* **2019**, *16*, 2737. [[CrossRef](#)] [[PubMed](#)]
- Tarawneh, Q.Y.; Chowdhury, S. Trends of Climate Change in Saudi Arabia: Implications on Water Resources. *Climate* **2018**, *6*, 8. [[CrossRef](#)]
- Friedlingstein, P.; Jones, M.W.; O’Sullivan, M.; Andrew, R.M.; Hauck, J.; Peters, G.P.; Peters, W.; Pongratz, J.; Sitch, S.; Le Quéré, C.; et al. Global Carbon Budget 2019. *Earth Syst. Sci. Data* **2019**, *11*, 1783–1838. [[CrossRef](#)]
- Bernauer, T.; Böhmelt, T. International conflict and cooperation over freshwater resources. *Nat. Sustain.* **2020**, *3*, 350–356. [[CrossRef](#)]
- Deng, Y.; Zhao, R. Advanced Oxidation Processes (AOPs) in Wastewater Treatment. *Curr. Pollut. Rep.* **2015**, *1*, 167–176. [[CrossRef](#)]
- Ghernaout, D. Advanced Oxidation Processes for Wastewater Treatment: Facts and Future Trends. *OALib* **2020**, *7*, 1–15. [[CrossRef](#)]
- Prieto-Rodríguez, L.; Oller, I.; Klamerth, N.; Agüera, A.; Rodríguez, E.M.; Malato, S. Application of solar AOPs and ozonation for elimination of micropollutants in municipal wastewater treatment plant effluents. *Water Res.* **2013**, *47*, 1521–1528. [[CrossRef](#)]
- Vogelpohl, A. Applications of AOPs in wastewater treatment. *Water Sci. Technol.* **2007**, *55*, 207–211. [[CrossRef](#)]
- Herrmann, J.M. Photocatalysis. In *Kirk-Othmer Encyclopedia of Chemical Technology*; John Wiley & Sons, Inc.: Hoboken, NJ, USA, 2017; pp. 1–44.
- Grätzel, M.; Rotzinger, F.P. The influence of the crystal lattice structure on the conduction band energy of oxides of titanium(IV). *Chem. Phys. Lett.* **1985**, *118*, 474–477. [[CrossRef](#)]
- Jaiswal, R.; Bharambe, J.; Patel, N.; Dashora, A.; Kothari, D.; Miotello, A. Copper and Nitrogen co-doped TiO₂ photocatalyst with enhanced optical absorption and catalytic activity. *Appl. Catal. B Environ.* **2015**, *168*, 333–341. [[CrossRef](#)]
- Mathew, S.; Ganguly, P.; Rhatigan, S.; Kumaravel, V.; Byrne, C.; Hinder, S.J.; Bartlett, J.; Nolan, M.; Pillai, S.C. Cu-Doped TiO₂: Visible Light Assisted Photocatalytic Antimicrobial Activity. *Appl. Sci.* **2018**, *8*, 2067. [[CrossRef](#)]
- Ren, F.; Li, H.; Wang, Y.; Yang, J. Enhanced photocatalytic oxidation of propylene over V-doped TiO₂ photocatalyst: Reaction mechanism between V5+ and single-electron-trapped oxygen vacancy. *Appl. Catal. B Environ.* **2015**, *176*, 160–172. [[CrossRef](#)]
- Kumaravel, V.; Rhatigan, S.; Mathew, S.; Bartlett, J.; Nolan, M.; Hinder, S.J.; Sharma, P.K.; Singh, A.; Byrne, J.A.; Harrison, J.; et al. Indium-Doped TiO₂ Photocatalysts with High-Temperature Anatase Stability. *J. Phys. Chem. C* **2019**, *123*, 21083–21096. [[CrossRef](#)]
- Liqiang, J.; Xiaojun, S.; Baifu, X.; Baiqi, W.; Weimin, C.; Honggang, F. The preparation and characterization of La doped TiO₂ nanoparticles and their photocatalytic activity. *J. Solid State Chem.* **2004**, *177*, 3375–3382. [[CrossRef](#)]
- Ahmed, S.N.; Haider, W. Heterogeneous photocatalysis and its potential applications in water and wastewater treatment: A review. *Nanotechnology* **2018**, *29*, 342001. [[CrossRef](#)] [[PubMed](#)]
- Loeb, S.K.; Alvarez, P.J.J.; Brame, J.A.; Cates, E.L.; Choi, W.; Crittenden, J.; Dionysiou, D.D.; Li, Q.; Puma, G.L.; Quan, X.; et al. The Technology Horizon for Photocatalytic Water Treatment: Sunrise or Sunset? *Environ. Sci. Technol.* **2018**, *53*, 2937–2947. [[CrossRef](#)] [[PubMed](#)]
- Orton, F.; Tyler, C.R. Do Hormone-Modulating Chemicals Impact on Reproduction and Development of Wild Amphibians? *Biol. Rev.* **2015**, *90*, 1100–1117. [[CrossRef](#)] [[PubMed](#)]
- Adeel, M.; Song, X.; Wang, Y.; Francis, D.; Yang, Y. Environmental impact of estrogens on human, animal and plant life: A critical review. *Environ. Int.* **2017**, *99*, 107–119. [[CrossRef](#)] [[PubMed](#)]
- Nasri, A.; Mezni, A.; Lafon, P.A.; Wahbi, A.; Cubedo, N.; Clair, P.; Harrath, A.H.; Beyrem, H.; Rossel, M.; Perrier, V. Ethinylestradiol (EE2) residues from birth control pills impair nervous system development and swimming behavior of zebrafish larvae. *Sci. Total Environ.* **2021**, *770*, 145272. [[CrossRef](#)]

24. Aris, A.Z.; Shamsuddin, A.S.; Praveena, S.M. Occurrence of 17α -ethynylestradiol (EE2) in the environment and effect on exposed biota: A review. *Environ. Int.* **2014**, *69*, 104–119. [[CrossRef](#)]
25. Murray, J.L.; Wriedt, H.A. The O–Ti (Oxygen-Titanium) system. *J. Phase Equilibria Diffus.* **1987**, *8*, 148–165. [[CrossRef](#)]
26. Sclafani, A.; Herrmann, J.M. Comparison of the Photoelectronic and Photocatalytic Activities of Various Anatase and Rutile Forms of Titania in Pure Liquid Organic Phases and in Aqueous Solutions. *J. Phys. Chem.* **1996**, *100*, 13655–13661. [[CrossRef](#)]
27. Shannon, R.D. Revised effective ionic radii and systematic studies of interatomic distances in halides and chalcogenides. *Acta Crystallogr. Sect. A Cryst. Phys. Diff. Theor. Gen. Crystallogr.* **1976**, *32*, 751–767. [[CrossRef](#)]
28. Thommes, M.; Kaneko, K.; Neimark, A.V.; Olivier, J.P.; Rodriguez-Reinoso, F.; Rouquerol, J.; Sing, K.S. Physisorption of gases, with special reference to the evaluation of surface area and pore size distribution (IUPAC Technical Report). *Pure Appl. Chem.* **2015**, *87*, 1051–1069. [[CrossRef](#)]
29. Engelhardt, T.B.; Schmitz-Stöwe, S.; Schwarz, T.; Stöwe, K. Development of A Novel High Throughput Photo-catalyst Screening Procedure: UV-A Degradation of 17α -Ethinylestradiol with Doped TiO₂-Based Photo-catalysts. *Materials* **2020**, *13*, 1365. [[CrossRef](#)]
30. Abramović, B.; Despotović, V.; Šojić, D.; Finčur, N. Mechanism of clomazone photocatalytic degradation: Hydroxyl radical, electron and hole scavengers. *React. Kinet. Mech. Catal.* **2014**, *115*, 67–79. [[CrossRef](#)]
31. Yanagida, S.; Nakajima, A.; Sasaki, T.; Kameshima, Y.; Okada, K. Processing and Photocatalytic Properties of Transparent 12 Tungsto(VI) Phosphoric Acid–TiO₂ Hybrid Films. *Chem. Mater.* **2008**, *20*, 3757–3764. [[CrossRef](#)]
32. Ohko, Y.; Hashimoto, K.; Fujishima, A. Kinetics of Photocatalytic Reactions under Extremely Low-Intensity UV Illumination on Titanium Dioxide Thin Films. *J. Phys. Chem. A* **1997**, *101*, 8057–8062. [[CrossRef](#)]
33. Attri, P.; Kim, Y.H.; Park, D.H.; Park, J.H.; Hong, Y.J.; Uhm, H.S.; Kim, K.-N.; Fridman, A.; Choi, E.H. Generation mechanism of hydroxyl radical species and its lifetime prediction during the plasma-initiated ultraviolet (UV) photolysis. *Sci. Rep.* **2015**, *5*, srep09332. [[CrossRef](#)] [[PubMed](#)]
34. Montgomery, D.C. *Design and Analysis of Experiments*, 7th ed.; Wiley: Hoboken, NJ, USA, 2009; ISBN 978-0-470-39882-1.